Precambrian Research 324 (2019) 208–219

Contents lists available at ScienceDirect

Precambrian Research

journal homepage: www.elsevier.com/locate/precamres

Geochemistry and petrogenesis of Archean mafic rocks from the Amsaga area, West African craton, Mauritania

Ashlea N. Wainwright*, Fatima El Atrassi, Vinciane Debaille, Nadine Mattielli

Laboratoire G-Time, Université Libre de Bruxelles (ULB), Belgium

ARTICLE INFO

Keywords:
Paleoarchean
^{142}Nd
West African Craton
Mauritania
Geodynamic regime

ABSTRACT

Determining the extent of mantle mixing during the Hadean-Archean is an integral factor in our understanding of early geodynamic processes as well as the speed and degree of mantle homogenisation. If a dynamic convecting mantle was the predominant regime it would be expected that early formed isotopic anomalies would be quickly homogenised, whilst in a stagnant lid regime these anomalies might last for hundreds of millions of years. Archean terranes are dominated by felsic tonalite, trondhjemite and granodiorite rocks, as such these rocks have been the main rock type studied, even though they are not formed by primary mantle melts. Therefore, in this study, we have focused on mafic rock samples as tracers of primary mantle melting, from the relatively unknown West African craton. The mafic rocks have undergone metamorphism to granulite facies with the majority of samples retrogressed to amphibolite facies. Major element compositions reveal that the protolith was tholeiitic basalt. The majority of trace elements display limited mobility, as primary correlations with Zr are still present. Trace element patterns are typical for Archean mafic rocks, with Nb-Ta and Ti depletions. The meta-basalts yield a ^{147}Sm-^{143}Nd errorchron with an age of 3300 ± 300 Ma, with initial εNd of +4.4. The Nd compositions indicate that the meta-basalts have experienced minimal crustal assimilation and retain primary geochemical attributes. A positive initial εNd for the meta-basalts suggests that the magmatic protolith evolved from an already differentiated source. Nevertheless, ^{142}Nd compositions are within error of modern day terrestrial, as such, the protolith for these samples either did not experience any early differentiation, or that mantle convection had homogenised any anomalous signal. These results highlight the lack of large (> ± 8 μ^{142}Nd) ^{142}Nd anomalies detected from outside the North Atlantic and Superior Cratons, suggesting that Archean mantle dynamics was complex, with different processes occurring on different parts of Earth, similar to today.

1. Introduction

The moon forming giant impact event created a global magma ocean which most likely resulted in early silicate differentiation events and the formation of a Hadean crust (Bourdon and Caro, 2007; Caro et al., 2005; Rizo et al., 2011). By tracing the recycling of this early formed crust, we can determine how dynamic the early mantle was to better understand the Earth's evolution (Bennett et al., 2007; Debaille et al., 2013). Short-lived radiogenic systems such as the ^{182}Hf-^{182}W and ^{146}Sm-^{142}Nd are the primary tools used for tracing Hadean and Archean differentiation events and subsequent mixing (Bennett et al., 2007; Boyet and Carlson, 2006; O'Neil et al., 2008; Puchtel et al., 2016; Rizo et al., 2011; Roth et al., 2013; Touboul et al., 2012; Willbold et al., 2015). Results from the ^{146}Sm-^{142}Nd system indicate that the oldest rocks on Earth display anomalous ^{142}Nd compared to the modern Earth, yet by the Neoarchean there are very limited accounts of anomalous ^{142}Nd signatures (Debaille et al., 2013). However, the Paleoarchean displays a wide range in ^{142}Nd compositions, from which Bennett et al. (2007) inferred two different models for the early silicate differentiation of the Earth either 1) a dynamic Earth where the mantle is stratified into an enriched and a depleted reservoir which is slowly mixed into a homogenous mantle by the Neoarchean, with Paleoarchean rocks sampling different portions of the dynamically mixed mantle or 2) a heterogeneously depleted Earth where the Earth accreted two distinctly different domains that remained separated due to inefficient mixing of the mantle, such that Paleoarchean rocks are sourced from these two distinct and separate domains. As such, the two different models would require distinctly different geodynamic regimes to be operating during the Archean, either a dynamically convecting mantle that interacts with the crust or a stagnant lid model where there is limited exchange with the underlying mantle. Indeed, Debaille et al. (2013) and O'Neill and Debaille (2014) have shown that a stagnant-lid regime during the

* Corresponding author at: School of Earth, Atmosphere and Environment, Monash University, Clayton, Australia.
E-mail address: ashlea.wainwright@monash.edu (A.N. Wainwright).

https://doi.org/10.1016/j.precamres.2019.02.005
Received 28 September 2018; Received in revised form 24 January 2019; Accepted 7 February 2019
Available online 08 February 2019
0301-9268/ © 2019 Elsevier B.V. All rights reserved.

Archean would imply a poorly-mixed mantle, while mantle mixing is enhanced in a mobile-lid regime. As such, it is possible to determine which geodynamical regime was likely operating based on geochemical and field information of Archean mafic rocks.

The geodynamical setting which formed Archean crust is heavily debated, with some geochemical signatures similar to modern arc related rocks, while field relationships generally indicate that these sequences are not arc-related. Consequently, there are two prevailing theories for the dominant geodynamical regime operating in the Hadean and Eoarchean: 1) a dynamic lid regime, in which arc-like complexes are formed via an accretionary process i.e. horizontal regime (Bédard, 2018; Moyen and van Hunen, 2012), or 2) a stagnant lid regime, where greenstone and TTG terranes are formed in an oceanic plateau situated over a rising mantle plume i.e. a vertical regime (Johnson et al., 2014, 2017; O'Neill and Debaille, 2014). Melting by impacts should also be taken into account for triggering melting in case of stagnant lid regime (Johnson et al., 2018).

A dynamic regime involves horizontal motion of the crustal plate resulting in either subduction (Moyen and van Hunen, 2012) or subcretion tectonics (Bédard et al., 2013). Subduction tectonics in the Archean could also have behaved similarly to today, but only as sporadic pulses rather than continuous subduction (Debaille et al., 2013). Subduction requires the lower plate to be the main driving force, as negatively buoyant lithosphere sinks into the asthenosphere under its own weight, obducting the overlying plate. This creates arc-like terranes with a true arc lithology sequence including basalts, calc-alkaline rocks and sediments. Of all the Archean cratons only three have been found to contain terranes that display all the attributes required to be an arc sequence (Greenland: Szilas et al., 2012; Yilgarn: DeJoux et al., 2014; Pilbara: Smithies et al., 2005). As such, this type of tectonic regime cannot account for other sequences such as the Acasta and Nuvvuagittuq Archean terranes. Therefore, the subcretion scenario was posited by Bedard (2013 and 2018), where the overriding continental plate is the main driving force, such that the buoyant oceanic lithospheric plate is partly overridden, and then accreted to, the drifting continents. This would allow for the formation of calc-alkaline sequences and for them to be interspersed with the primary mafic compositions in arc-like sequences. Both of the horizontal regimes would require a moderately to strongly convecting mantle to enable continental drift, the subduction or foundering of the oceanic lithosphere would result in quick mantle mixing times.

In a vertically dominated regime, the hot and ductile crust is unable to break and be subducted such that it is stagnant and the crust remains isotopically isolated from the mantle for long periods of time (Johnson et al., 2014; Korenaga, 2008; O'Neill and Debaille, 2014). Subsequent destruction of this crust by impact, mantle overturns, sagduction or foundering can be traced by the mixing of the two isotopically distinct signatures in consequent primary mafic melts. Under a stagnant lid regime, this mixing would be a sluggish process with slow mixing times, such that isotopic signatures from short-lived radionuclides are preserved (Debaille et al., 2013; O'Neill et al., 2013; O'Neill and Debaille, 2014). Evidence for long mixing times are seen in the anomalous ^{182}W of 2.8 Ga komatiites and ^{142}Nd of 2.7 Ga tholeiities (Debaille et al., 2013; Touboul et al., 2012), indicating that an early formed source reservoir was retained for over 1.6 Ga. These two isotopic systems record different types of differentiation (metal-silicate versus silicate-silicate respectively), such that the preservation of both anomalous reservoirs for similar periods of times is difficult to address by resorting to hidden reservoirs in a dynamically convecting mantle.

Trace element characteristics between Archean rocks and their modern equivalents have been used as possible evidence for both vertical and horizontal regimes. However, there are a number of unknown variables regarding the Archean mantle that could affect trace element fractionation, for example the higher ambient mantle temperature at depth will potentially change the mineralogy present and the trace element partitioning during mantle melting. As such, Condie (2015) advises that determining the geodynamical regime of Archean rocks should not be limited to geochemical characteristics and should include field relationships and presence of certain lithologies as well. Such studies of Archean terranes have been confined to the well-known TTG (tonalite, trondhjemite and granodiorite) and greenstone belts of the Kaapvaal, Pilbara, Yilgarn, Superior and North Atlantic cratons (Bennett et al., 2007; Boyet and Carlson, 2006; Caro et al., 2017; O'Neil et al., 2008; Rizo et al., 2011; Roth et al., 2013) limiting the amount of information available to geographically restrained areas.

The present study aims to investigate the chemical evolution of the Earth's mantle with time through the geochemical characteristics of a suite of mafic rocks from the Amsaga area, West African craton, Mauritania. We will present new whole-rock major and trace elements, and ^{147,146}Sm–^{143,142}Nd isotopic data for these Archean mafic rocks. It is the first time that the isotopic characteristics of Archean mafic rocks from the West African Craton have been determined. We show that these rocks display high initial ε^{143}Nd and yet have no anomalous μ^{142}Nd isotopic signatures, indicating that they were differentiated from a depleted reservoir possibly generated after the extinction of ^{146}Sm.

2. Geological setting

The West African craton is exposed in two distinct zones: the Reguibat rise in the north (Morocco, Algeria, and Mauritania) and the Leo-Man rise in the south (from Liberia to Ghana, through Guinea, Mali, Ivory Coast and Burkina Faso). These two zones are surrounded by sedimentary basins, the Tindouf basin in the north and the Taoudeni basin in the south. The Reguibat and Leo-Man rises are composed of Archean formations in the west and Proterozoic formations in the east. The Proterozoic parts of these two domains have been well studied (Abouchami et al., 1990; Boher et al., 1992). However, the Archean areas have received limited attention (Potrel, 1994; Key et al., 2008; Berger et al., 2013).

This study focuses on the Amsaga area of the Reguibat rise in Mauritania (Fig. 1). This region is part of the Choum-Rag el Abiod terrane (Key et al., 2008), located in the south-east of the Reguibat rise. Amsaga is formed of typical lithologies for Archean terranes, namely TTG and migmatitic orthogneiss associated with mafic and sedimentary rocks (metapelites and metagraywackes). This region also contains ultramafic rocks (anorthosites, chromitites) as well as ferruginous quartzites, marbles and banded iron formations (BIFs). The northern zone of Amsaga is intruded by 2.99 Ga charnockitic gneiss plutons (Potrel, 1994; Potrel et al., 1998; Berger et al., 2013). Other than the addition of volumetrically minor Paleoproterozoic doleritite dykes, the Amsaga area has not undergone any major volcanic or tectonic events since 2.7 Ga (Potrel, 1994; Potrel et al., 1998; Berger et al., 2013).

The gneisses in the Amsaga area have been dated to between 3.50 and 3.40 Ga (Auvray et al., 1992; Potrel, 1994; Potrel et al., 1996), with the oldest U-Pb zircon ages of an orthogneiss of 3515 ± 15 Ma and 3422 ± 10 Ma (Potrel et al., 1996). The last tectono-thermal event experienced by Amsaga was due to the emplacement of a 2.7 Ga gabbros (the Iguilid and Guelb el Azib gabbros, Potrel et al., 1998) and a 2.7 Ga granitic pluton (the Touijenjert granite, Auvray et al., 1992; Potrel et al., 1998). The Iguilid gabbro has a negative initial εNd (–0.7) likely indicating a complex history likely involving crustal contamination during emplacement. The two gabbros, Iguilid and Guelb el Azib, represent the only mafic rocks studied and dated in the Amsaga area, despite the prevalence of numerous Archean mafic rocks.

3. Field characteristics and petrography

The Amsaga is a desert with well-preserved outcrops, due to the absence of vegetation and a dry climate. The mafic rocks represent one of the dominant lithologies in the Amsaga area and were sampled from fresh exposures. The rock is typically dark-coloured, foliated and shows

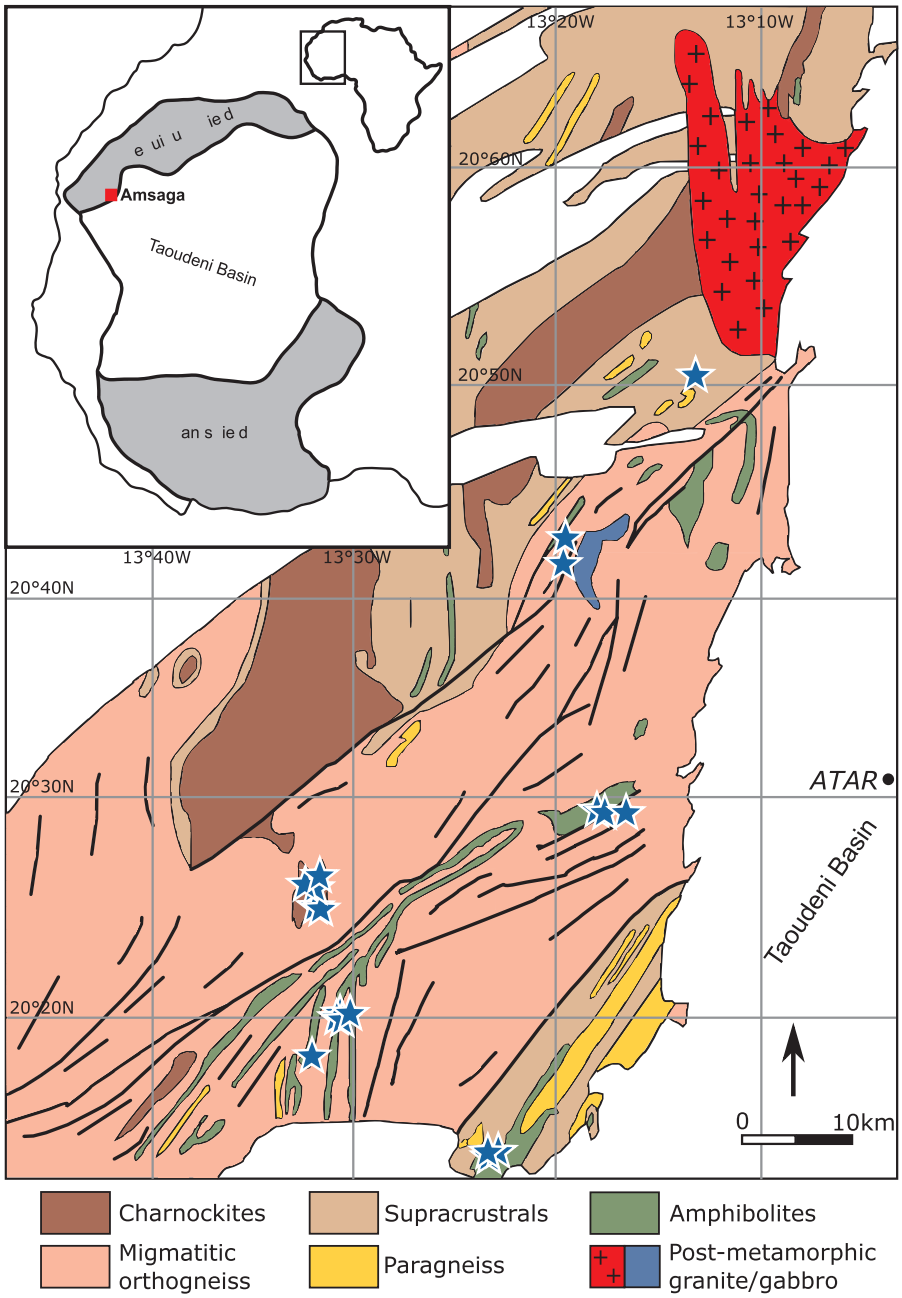

Fig. 1. Map of the Amsaga area in Mauritania. Inset shows location of Amsaga in Africa. Blue stars represent sample localities.

schistose structure (Fig. 2). The mafic rocks for this study were collected from different localities in the Amsaga area. Forty thin sections were prepared and examined under the microscope.

In this study we avoided samples showing obvious hydrothermal alteration recorded by the presence of saussuritisation of plagioclase, silicification and metasomatism, as observed through the addition of hydrous veins/minerals.

The Archean mafic rocks in the Amsaga area are exposed either as massive exposures (Fig. 2c), as layers affected by the same foliation as the surrounding rock (generally orthogneiss) (Fig. 2a, b, d), or also as lenses. The layers are typically 0.5 to 10 m in thickness with both sharp and gradual contacts observed between the mafic rocks and the surrounding gneisses (Fig. 2a and b). Quartz veins of varying width traverse the mafics at many places hosting visible sulphide minerals (mainly pyrite).

The mafic rocks range from fine to coarse-grained and typically have granoblastic and porphyroblastic textures (Fig. 3a). They are composed primarily of amphibole and plagioclase in similar proportions with lesser amounts of orthopyroxene, clinopyroxene, quartz, biotite, and apatite in some samples (Fig. 3). A few samples show foliation, and occasionally amphibole and plagioclase occur as needle-like crystals with a preferred orientation.

4. Analytical methods

4.1. Whole-rock major and trace element analysis

After careful petrographic study, samples with minimal alteration were chosen for geochemical analysis, with fresh unaltered samples analysed for major and trace elements, ^{142}Nd and ^{143}Nd.

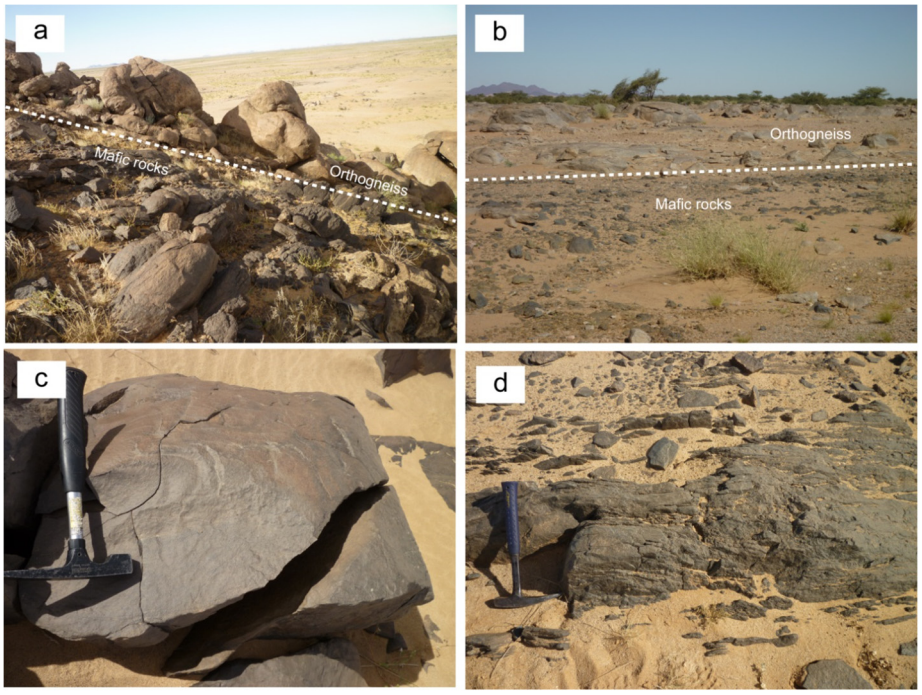

Fig. 2. Field photographs of mafics rocks from the Amsaga area: (a) and (b) contact between mafic rocks and the surrounding orthogneiss; (c) mafic rocks with massive structures; (d) mafic rocks with schistose structures.

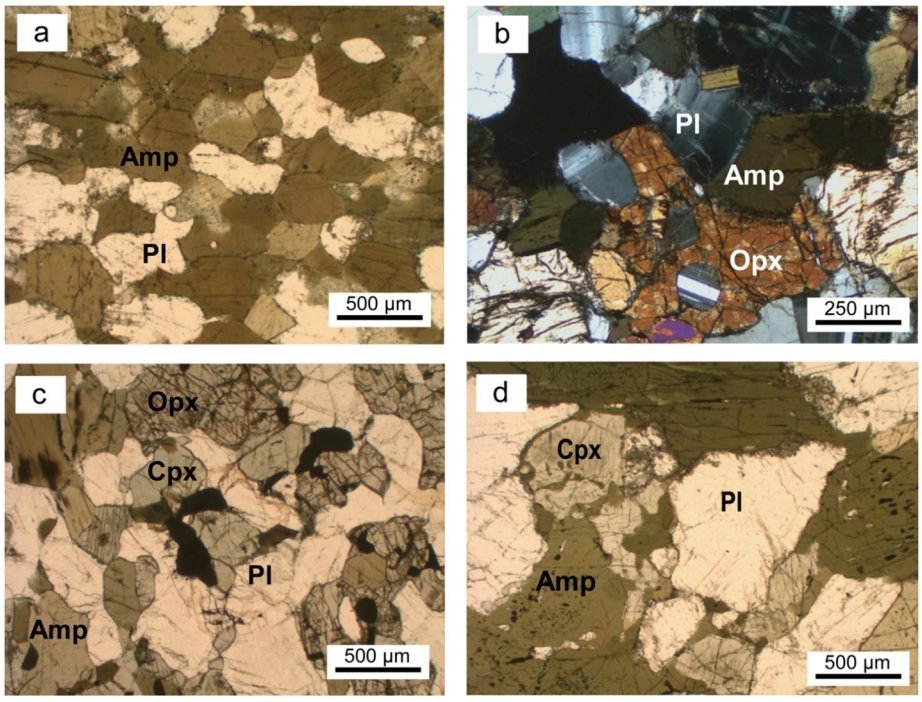

Fig. 3. Photomicrographs of mafic rocks from the Amsaga area: (a) massive mafic rock with a granoblastic texture; (b) orthopyroxene containing small amphibole inclusions; (b) (c) amphibole, plagioclase, clinopyroxene, orthopyroxene grains display sharp to rounded boundaries; (d) amphibole progressively replaces clinopyroxene.

Samples were crushed and pulverized using an agate mill at the Laboratoire G-Time at the Université Libre de Bruxelles (ULB), Belgium. Major elements were obtained on powder aliquots after alkaline fusion, on a Thermo Fischer iCAP ICP-OES. For that, around 50 mg of samples were mixed with high purity lithium metaborate flux in a graphite crucible and heated for 10 min at 1000 °C. After cooling, the bead was dissolved for several hours using a stirring magnet in 5% HNO_3. After dilution, the samples were measured with USGS standards BHVO-2 and AGV-2 were used as unknown standards to evaluate precision, which is better than 2% (2RSD) for each element. Loss on ignition was obtained after 1 h at 1000 °C.

Trace elements were analysed with an Agilent 7700 Q-ICP-MS at the Laboratoire G-Time (ULB). Approximately 100–120 mg of powdered samples were dissolved using concentrated acid (HF + HNO_3 followed by HCl) in sealed Savillex beakers on a hot plate at 120 °C for four days with evaporation and re-dissolution between the two acid steps. Analyses were conducted using a He collision cell and samples were introduced with 5% HNO_3. Standards BHVO-2 and BCR-2 were used as international reference material.

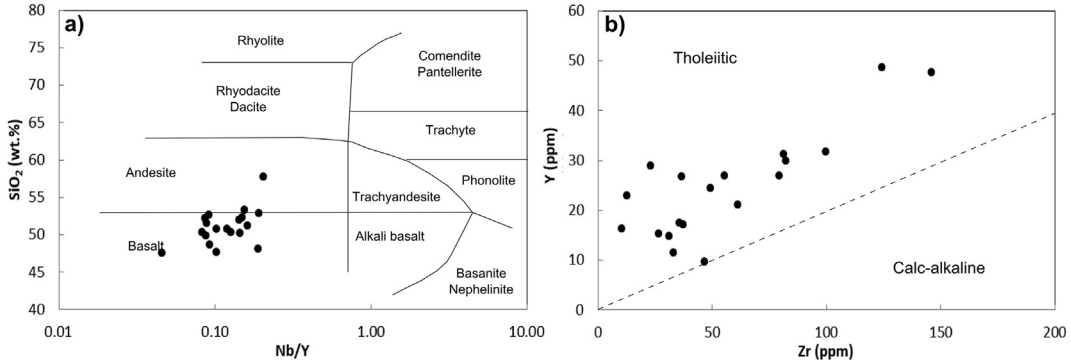

Fig. 4. (a) Nb/Y versus SiO_2 (wt%) classification diagram; (b) Zr (ppm) versus Y (ppm) for mafic rocks from the Amsaga area. Diagrams are from Winchester & Floyd (1977).

4.2. Whole-rock Sm–Nd isotope analysis

Initially nineteen mafic samples were analysed for ^{143}Nd by MC-ICPMS (Multi-Collector Inductively Coupled Plasma Mass Spectrometer), six of these were repeated and analysed for ^{142}Nd by TIMS (Thermal Ionisation Mass Spectrometer).

For analysis by MC-ICPMS, samples were weighed and digested using a mixture of concentrated HNO_3-HF followed by HCl. Neodymium was purified from the matrix using a two-column ion-exchange technique as detailed in Debaille et al. (2013). After digestion a 5% aliquot was taken for isotope dilution analysis of Nd, and Sm with a ^{150}Sm-^{148}Nd mixed spike. For both spiked and unspiked samples, first, the rare earth elements (REE) were extracted from the sample using ~2 ml of AG50W-X8 cation resin (200–400 mesh). Then HDEHP (di-2ethylhexyl-orthophosphoric acid)-coated Teflon powder was used for purifying Nd from Sm and Ce, both of which cause isobaric interferences.

For ^{142}Nd measurements, samples were digested in closed Savillex beakers in a HNO_3-HF mix followed by digestion in HCl. The separation procedure used was adapted from Debaille et al. (2007). Five separate columns are used to purify Nd from Ce and Sm. Firstly, a large anion (AG1X8) column is used for the removal of Fe to avoid over-loading any subsequent columns. The subsequent two columns are the same as those detailed above for the ^{143}Nd analysis, namely a cation column for separation of the REE, followed by a HDEHP-coated Teflon powder column for the separation of Nd from Sm and Ce. For ensuring an efficient removal of Ce from the Nd cut, a solvent extraction step was performed, using the procedure of Li et al. (2014) to remove Ce oxidised as Ce^{4+} on a second HDEHP column. By oxidising the Ce in the loading solution (10 N HNO_3 + 10 mmol $NaBrO_3$) it is retained on the column resulting in a very pure Nd cut. The final column is a scaled down version of the first cation column, using only 0.5 ml of AG50X8 resin, to remove the Na added during the Ce clean-up column. Total procedural blanks are < 50 ppt for Nd and < 5ppt for Sm.

The ^{143}Nd samples and the spiked aliquots for Sm and Nd, were measured using a high-resolution Nu Instruments Plasma I MC-ICPMS at the Laboratoire G-Time (ULB). The isotopic ratios were measured by static multi-collection in dry plasma with an Aridus II desolvator. For ^{143}Nd each analysis consists of 3 blocks of 20 runs each. The repeated measurements of Rennes international standard gave an external reproducibility of 16 ppm (2σ, n = 20). Neodymium isotopic compositions were corrected by internal normalization to the value of $^{146}Nd/^{144}Nd = 0.7219$, and by sample-standard bracketing using the recommended value of the Rennes standard ($^{143}Nd/^{144}Nd = 0.511961$; Chauvel & Blichert-Toft, 2001). Total blank was negligible (8 pg) and reproducibility was better than 99% as measured over seven replicate analyses. For analysis of spiked Sm and Nd the mass fractionation factors for each element were derived by solving iteratively non-linear equations combining the exponential fractionation law and the spike-natural mixing equations as in Debaille et al. (2007).

High precision ^{142}Nd was measured with a Thermo Scientific Triton Plus TIMS at the Laboratoire G-Time (ULB). Samples were measured as Nd metal on Re double filaments. Total measurements consisted of 18–45 blocks of 20 cycles, with an intensity on ^{142}Nd greater than 3 V. Each measurement cycle consisted of a multi-static sequence across 3-lines following the method of Caro et al. (2006) to ensure that all isobaric interferences could be monitored. Isobaric interferences from Sm and Ce were minimal, with the largest Ce correction applied of 1 ppm and no ^{147}Sm was detectable. International reference materials Ames and JNdi were run alongside the samples, with long term reproducibilities of 1.141831 ± 2 (2SD; n = 5) for Ames and 1.141834 ± 6 (2SD; n = 13) for JNdi.

5. Results

5.1. Whole-rock major and trace element compositions

The Amsaga mafic rocks show a range of major element compositions with 47.61–53.31 wt% SiO_2, 0.45–2.21 wt% TiO_2, 12.05–21.71 wt % Al_2O_3, 7.59–19.78 wt% CaO, 7.06–18.44 wt% Fe_2O_{3T} and 3.35–8.91 wt% MgO. Mg# ($Mg\# = 100 \times (Mg^{2+} / (Mg^{2+} + Fe^{2+}))$) are low ranging between 33.4 and 62.3% (average 46.25 ± 8.6). The SiO_2, Nb/Y, Y and Zr contents of the Amsaga mafic rocks indicate that their protolith was a tholeiitic basalt (Fig. 4). As such, hereafter the Amsaga mafic rocks will be referred to as 'meta-basalts'. Major elements show a very weak correlation with Mg# (Fig. 4), while the REE and HFSE display a strong positive correlation with Zr (Fig. 6).Fig. 5Fig. 6

Normalized to chondrite, the REE display near-flat to moderately enriched LREE patterns (La_N/Sm_N = 1.06–2.10; La_N/Yb_N = 1.13–2.26; where N designates normalization to chondrite from Anders and Grevesse (1989)), with only slightly fractionated HREE patterns (Gd_N/Yb_N = 1.03–1.61). There are two exceptions where LREE and HREE fractionations are seen (La_{PM}/Sm_{PM} = 3.74 and 4.32 Gd_{PM}/Yb_{PM} = 1.52 and 1.42). The majority of samples display limited Ce and Eu anomalies, with one minor negative Eu anomaly of 0.81 and three with a positive Eu anomaly between 1.15 and 1.21 (Table 1). On primitive mantle-normalized diagrams these mafic rocks display a depletion of Ti relative to MREE (Fig. 7; Ti_{PM}/Sm_{PM} = 0.36–0.83 where PM designates normalization to primitive mantle from McDonough and Sun, (1995)) and negative Nb and Ta anomalies (Nb/Nb*: 0.22–0.78; Table 1). Their Nb/Ta and Ti/Zr ratios vary from 6.25 to 13.61 and from 36 to 103 respectively.

5.2. Sm-Nd systematics

The majority of the Amsaga meta-basalts have a narrow range in $^{143}Nd/^{144}Nd$ compositions with 17 of the samples ranging between 0.511100 and 0.512850 (Table 2). No significant difference was seen

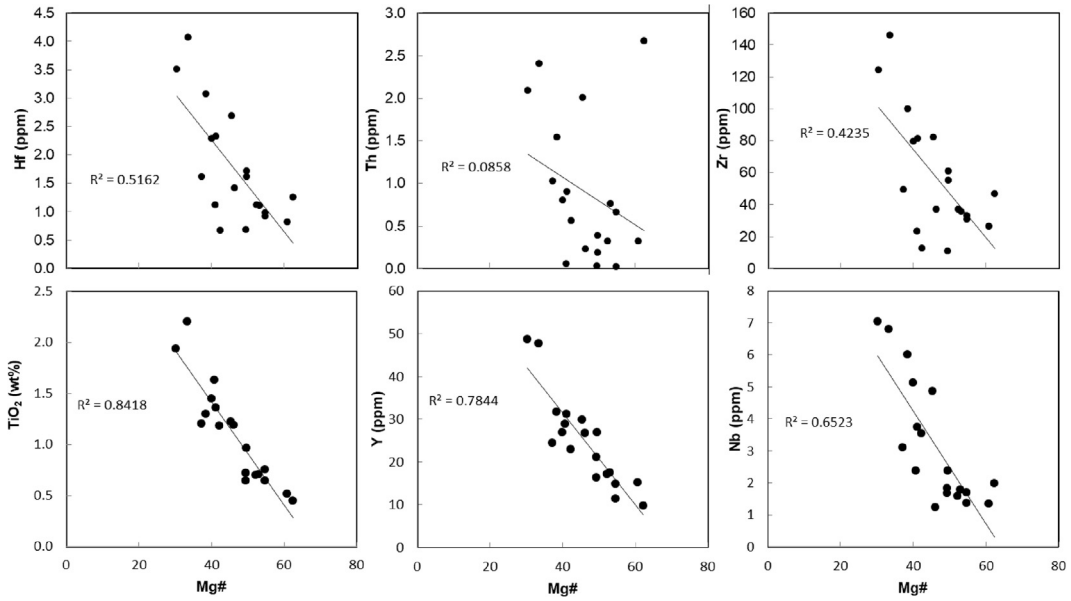

Fig. 5. Two element diagrams, with minor elements versus Mg#. TiO_2, Y, Nb show strong correlations, Hf and Zr also correlate but to a smaller degree, indicating that they have not been affected by post emplacement process and still display their primary melting features. Th shows no correlation indicating that it has been strongly modified by post crystallisation processes.

between the $^{143}Nd/^{144}Nd$ compositions obtained by MC-ICPMS or TIMS. However, because the two datasets are characterized by so different internal errors and as the values obtained on the Nu-Plasma have been normalized to a different standard, the 6 values obtained on the TIMS will only be considered for the ^{142}Nd systematics and not for the ^{143}Nd one.

The $^{147}Sm/^{144}Nd$ compositions show a similar trend, with the 5 clustered samples ranging between 0.1666 and 0.1776 with two outliers at 0.1144 and 0.1918 respectively. For ^{142}Nd all of the samples are within error of modern day terrestrial with $\mu^{142}Nd$ from −3.50 to 3.79 ± 4 (Table 2), where μ is defined as

$$\mu^{142}Nd = \left(\frac{\frac{^{142}Nd}{^{144}Nd_{sample}}}{\frac{^{142}Nd}{^{144}Nd_{standard}}} - 1 \right) \times 10^6$$

where the standard is the JNdi reference standard run in the same

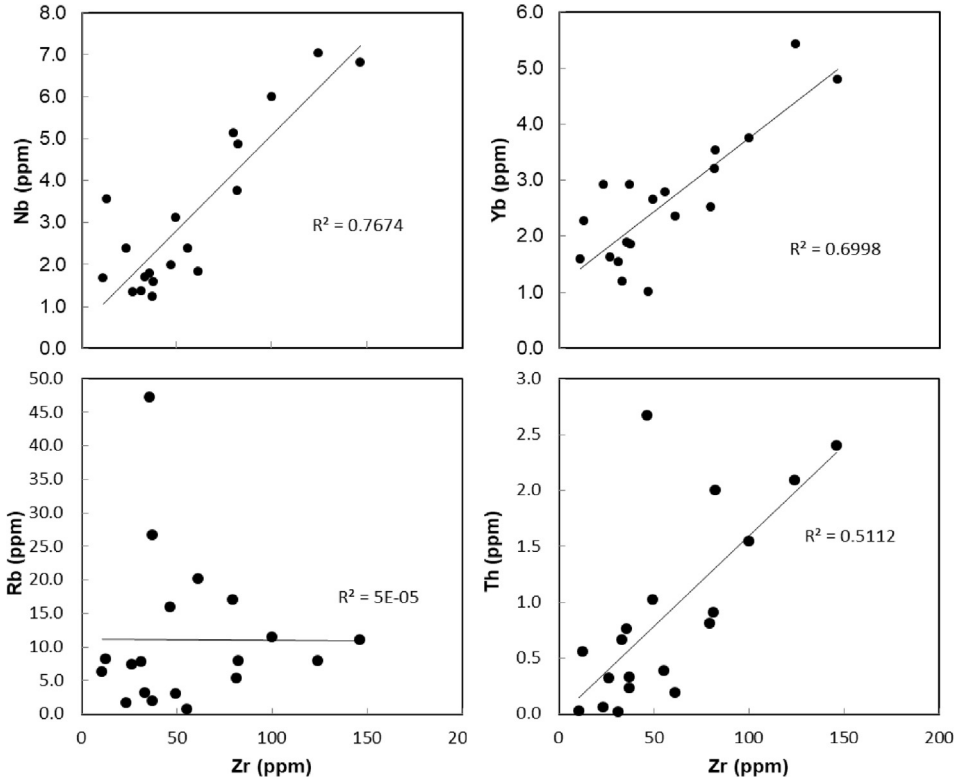

Fig. 6. Two element diagrams of minor elements versus Zr, the majority of elements show no post emplacement modification, however Th and Rb show no correlation, highlighting their fluid mobility and indicating that they have been modified from their primary compositions.

Table 1
Major and trace element compositions of the Amsaga meta-basalts

Sample	M13_5b	M13_32a-1	M13_37	M13_42	M13_43c	M13_43d	M13_54a	M13_58	M13_64a	M13_64b	M13_64c	M13_64e	M13_68b	M13_77b	M13_76a	M13_84	M13_101	M13_102	M13_105
Al_2O_3	13.58	15.26	12.87	21.71	13.25	13.84	14.78	13.00	13.83	14.42	12.05	13.97	15.55	12.78	12.68	14.67	13.44	16.58	14.10
CaO	9.84	9.62	7.59	13.84	11.25	11.21	9.39	19.78	18.88	14.11	10.72	10.94	9.93	10.78	10.49	11.56	9.97	10.16	13.02
Cr_2O_3	0.02	0.01	0.00	0.01	0.02	0.05	0.02	0.03	0.03	0.02	0.13	0.05	0.04	0.02	0.01	0.03	0.02	0.02	0.04
Fe_2O_3	14.52	13.95	18.44	7.06	13.10	12.08	8.08	10.09	10.22	14.28	10.26	11.96	12.34	14.88	16.19	13.15	14.96	10.14	12.02
K_2O	0.54	1.07	0.47	0.28	0.61	0.22	0.94	0.09	0.67	0.43	0.24	0.15	0.76	0.64	0.20	0.26	0.25	0.39	0.04
MgO	5.08	8.84	5.18	3.87	5.37	6.62	7.50	3.35	4.90	3.48	8.91	7.32	4.60	6.93	6.26	8.89	5.86	6.87	6.62
MnO	0.19	0.25	0.31	0.10	0.22	0.18	0.13	0.39	0.22	0.38	0.16	0.20	0.18	0.22	0.23	0.19	0.22	0.14	0.10
Na_2O	3.15	2.04	2.36	2.89	3.09	2.96	3.69	0.75	1.14	1.58	2.47	3.15	0.98	2.64	2.79	2.05	2.67	3.17	1.09
P_2O_5	0.08	0.02	0.16	0.05	0.07	0.03	0.04	0.07	0.08	0.13	0.02	0.03	0.08	0.07	0.10	0.03	0.08	0.03	0.05
SiO_2	48.14	47.64	51.98	50.82	53.31	52.18	57.78	50.38	47.61	50.20	49.90	52.64	52.86	51.25	50.28	48.71	50.73	52.37	51.56
TiO_2	1.30	0.71	2.21	0.65	1.18	0.72	0.45	1.20	1.19	1.94	0.52	0.70	1.45	1.22	1.63	0.75	1.36	0.65	0.97
Total	96.45	99.42	101.57	101.25	101.48	100.09	102.78	99.13	98.77	100.98	95.37	101.12	98.78	101.43	100.86	100.29	99.56	100.51	99.62
LOI, %	3.08										2.60								
Co	50.94	52.88	42.92	29.55	52.70	39.87	29.77	46.67	48.33	40.88	46.30	44.29	38.22	61.97	50.48	60.36	46.36	43.30	33.41
Ni	68.96	190.60	53.39	79.09	66.89	71.11	69.54	91.73	93.34	53.99	81.89	73.77	41.18	83.34	56.29	141.05	63.69	128.92	102.91
Cu	127.62	9.71	62.71	40.10	26.23	9.74	29.63	4.69	15.57	33.07	18.34	68.53	7.88	145.13	89.40	3.14	78.03	46.57	8.13
Zn	98.57	146.75	293.04	49.52	178.49	78.38	50.13	93.69	109.78	113.50	63.37	46.98	139.82	108.73	110.44	94.11	116.12	77.95	74.53
Ga	43.43	103.98	103.63	15.34	17.14	48.03	51.33	21.59	16.46	106.36	21.56	55.48	98.50	28.93	17.43	13.33	40.83	68.84	24.27
Ge	3.21	2.59	4.12	1.87	3.68	2.15	2.06	3.06	2.52	3.27	3.01	2.89	2.96	3.14	4.43	2.65	3.23	2.27	3.32
Rb	11.52	47.19	11.11	6.24	8.12	20.17	15.96	2.97	26.74	7.97	7.37	1.96	17.07	7.94	1.64	7.75	5.29	3.22	0.73
Sr	117.55	117.57	72.01	129.51	153.83	176.88	177.95	182.34	223.75	140.33	96.27	84.40	111.80	131.15	117.58	110.64	118.32	305.40	483.01
Y	31.79	17.50	47.73	16.29	22.88	21.07	9.70	24.37	26.81	48.66	15.25	17.17	26.87	29.94	28.87	14.81	31.24	11.44	26.95
Zr	99.83	35.67	146.16	10.75	12.84	61.17	46.59	49.32	37.01	124.28	26.56	37.25	79.42	82.14	23.26	31.08	81.39	33.05	55.43
Nb	6.00	1.79	6.81	1.67	3.55	1.82	1.98	3.10	1.23	7.04	1.34	1.58	5.12	4.87	2.38	1.37	3.75	1.71	2.38
Cd	0.12	0.04	0.09	0.08	0.10	0.04	0.00	0.02	0.18	0.05	0.05	0.02	0.14	0.07	0.17	0.14	0.08	0.02	0.02
Ba	215.40	722.25	592.83	127.44	187.93	280.49	316.16	67.22	295.69	676.70	83.17	335.77	601.60	108.63	35.72	30.04	197.03	414.60	78.69
Hf	3.07	1.11	4.07	0.68	0.67	1.71	1.25	1.61	1.41	3.51	0.82	1.12	2.29	2.69	1.12	0.98	2.32	0.92	1.61
Ta	0.52	0.21	0.50	0.17	0.28	0.14	0.15	0.31	0.12	0.68	0.16	0.15	0.44	0.78	0.18	0.13	0.29	0.16	0.18
Pb	4.18	4.44	6.16	5.01	6.01	5.38	1.71	1.18	6.04	4.19	5.61	1.92	4.43	3.73	1.23	1.78	2.10	2.60	6.87
Th	1.54	0.76	2.40	0.03	0.56	0.19	2.67	1.02	0.23	2.09	0.32	0.32	0.81	2.00	0.06	0.02	0.90	0.66	0.38
U	0.20	0.15	0.31	0.03	0.21	0.05	0.17	0.13	0.11	0.28	0.04	0.05	0.14	0.18	0.04	0.01	0.09	0.05	0.04
La	9.93	5.29	14.01	2.24	9.98	5.45	11.11	6.27	5.50	13.78	4.28	3.11	7.94	9.65	6.93	2.84	7.36	12.89	4.39
Ce	21.86	9.79	30.73	6.11	19.25	11.15	20.39	13.94	12.04	28.48	8.90	6.79	18.89	21.89	17.80	7.35	16.53	23.71	10.40
Pr	2.89	1.14	4.20	0.98	2.37	1.42	2.22	1.85	1.70	3.63	1.13	0.99	2.61	2.93	2.71	1.08	2.29	2.68	1.50
Nd	13.24	4.92	19.42	5.49	10.51	6.46	8.37	8.72	8.34	16.22	4.99	4.80	12.41	13.19	13.13	5.56	10.83	10.18	7.48
Sm	3.98	1.57	6.01	1.76	2.93	1.99	1.61	2.78	2.54	4.85	1.47	1.68	3.71	3.71	3.88	1.65	3.44	2.16	2.57
Eu	1.45	0.71	2.61	0.63	0.92	0.78	0.55	1.03	0.98	1.51	0.58	0.67	1.25	1.31	1.24	0.64	1.26	0.87	0.98
Gd	5.60	2.27	7.71	2.59	3.61	2.84	1.73	3.80	3.64	6.69	2.11	2.38	4.77	5.30	4.74	2.22	4.65	2.18	3.71
Tb	0.91	0.38	1.23	0.44	0.59	0.48	0.25	0.64	0.62	1.14	0.36	0.42	0.75	0.86	0.76	0.38	0.77	0.33	0.63
Dy	6.15	2.77	8.14	2.95	4.07	3.39	1.63	4.32	4.37	8.24	2.57	2.93	4.82	5.81	5.14	2.60	5.32	2.05	4.35
Ho	1.33	0.61	1.73	0.63	0.83	0.75	0.35	0.93	0.94	1.82	0.55	0.64	1.00	1.24	1.07	0.53	1.13	0.43	0.96
Er	3.92	1.83	5.00	1.79	2.46	2.28	0.99	2.78	2.85	5.56	1.65	1.88	2.89	3.66	3.10	1.62	3.30	1.19	2.88
Tm	0.57	0.27	0.71	0.24	0.34	0.34	0.14	0.39	0.41	0.81	0.23	0.28	0.40	0.53	0.43	0.23	0.47	0.17	0.41
Yb	3.75	1.89	4.79	1.59	2.26	2.36	1.01	2.65	2.91	5.43	1.62	1.85	2.53	3.53	2.91	1.54	3.20	1.19	2.78
Lu	0.53	0.27	0.69	0.23	0.32	0.36	0.15	0.38	0.44	0.79	0.22	0.27	0.35	0.48	0.42	0.21	0.48	0.16	0.41
Mg#	38.42	53.04	33.37	49.39	42.22	49.42	62.33	37.17	46.10	30.25	60.75	52.18	39.92	45.36	40.78	54.65	41.11	54.69	49.54

Major element oxides are in wt% and trace elements in ppm.

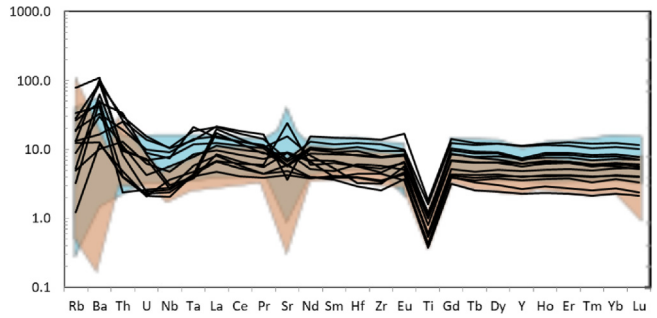

Fig. 7. Spider diagrams showing arc-like signatures for the Amsaga meta-basalts. Elements have been normalised to primitive mantle (McDonough and Sun, 1995). All samples display a Ti depletion and variable Nb-Ta depletions. Orange shaded area represents mafic rocks from the Isua Greenstone Belt, Greenland (Polat and Hofmann, 2003), blue shaded area represents mafic rocks from the Abitibi Greenstone Belt (Dostal and Mueller, 2013; Kerrich et al 1999, 2008; Wyman 1999).

sequence as the samples.

In $^{143}Nd/^{144}Nd$ – $^{147}Sm/^{144}Nd$ space, the Amsaga meta-basalts fall on a straight line. However, two of them (M13_37 and M13_58) are significantly further away from the regression line compared to other samples, and will not be considered in the calculation of the age. As no correlation is found between $^{143}Nd/^{144}Nd$ and 1/Nd, this regression line is interpreted as having a chronological meaning. Using Isoplot (version 4.15, Ludwig, 2003) an errorchron with an age of 3300 ± 300 Ma (2σ, MSWD = 20) is obtained, with an initial $^{143}Nd/^{144}Nd$ of 0.50857 (Fig. 8), corresponding to $\varepsilon Nd_i = +4.4 \pm 6.8$. Using the ages obtained for those 17 samples, initial εNd were calculated and range from +1.21 to +7.53 (Table 2).

6. Discussion

6.1. Geochemical signature of the protolith and effects of crustal contamination

Archean rocks have generally gone through a number of tectonothermal events that can modify the original geochemical signature of the rocks and make it difficult to determine what/if any primary signatures remain of the original protolith (Condie, 2015; Ordóñez-Calderón et al., 2008; Polat and Hofmann, 2003). The Amsaga meta-basalts are no exception to this, with the area having undergone at least one major deformation event at 2.7 Ga (Potrel et al., 1996, 1998) such that the original basalt protoliths have been metamorphosed to varying degrees of granulite and retrograde amphibolite facies. Petrographically, the Amsaga meta-basalts chosen for this study have limited accessory mineralisation, with no zircons or baddeleyite seen at the thin section level and minimal products of fluid alteration. However, this does not preclude the possibility that some elements have been remobilized during metamorphism. The degree of alteration that has affected these rocks can be assessed by examining the major and trace elements for effects of crustal assimilation and alteration.

Crustal contamination during the emplacement of the meta-basalts can be ruled out predominately due to their largely positive εNdi values. Due to the contrast in ^{143}Nd composition and Nd concentration between the melt and felsic country rock, any crustal assimilation will result in a decrease in the initial εNd values while also showing a correlation with other contamination sensitive elements and ratios (e.g. Si, Mg, Th/Ce, Nb/La, Ni, Cr, Th). While a decrease due to crustal assimilation could still result in a positive εNd value, the Amsaga meta-basalts report positive εNd_i values of +4.4 (see the errorchron) that are consistent with the depleted MORB mantle (DMM) at that time. However, these parameters only rule out contamination by continental crust, while it could be envisaged that these meta-basalts erupted through a mafic crust of similar composition to the magma, but thick enough to have the lowest part in the rutile stability field. As such, any contamination would be difficult to trace. Indeed, mixing between the source magma and the mafic crust would result in a trace element pattern similar to the original source magma, but may explain the Nb-Ta depletion. A thick mafic crust would have amphibole and rutile stable at depth, which would retain the Nb and Ta, such that mixing between the two sources would result in a Nb-Ta anomaly but still with Nb_{PM} and Ta_{PM} greater than 1. This option is discussed in more details in the next section.

Two-element plots with Mg# (Fig. 5), show that the HFSE and REE have been unaffected by most post-eruption processes, with the majority of elements showing primary melting features. However, the Al_2O_3 content does not change systematically with any other element, suggesting that the Al has been affected by the retrograde amphibolite grade metamorphism. This is not surprising given that Al is a major constituent of amphibole minerals. The extent of mobilisation of the fluid mobile elements such as Na, K, Ca, and LILE can be assessed by comparing them to the fluid immobile element Zr (Fig. 6; Polat and

Table 2
Sm and Nd Elemental and Isotopic data for the Amsaga meta-basalts.

Sample	Nd (ppm)	Sm (ppm)	$^{147}Sm/^{144}Nd$	$^{143}Nd/^{144}Nd$	2σ	$\varepsilon^{143}Nd_i$	$^{142}Nd/^{144}Nd$	2σ	$\mu^{142}Nd$	2σ
M13_5b	7.60	2.13	0.1696	0.512351	9	5.9	1.1418355	4E-06	3.8	3.2
M13_32a-1	3.85	1.13	0.1776	0.512483	7	5.1	1.1418297	3E-06	−1.3	2.8
M13_37*	1.49	0.37	0.1511	0.512225	5	11.4	n.a.	n.a.	n.a.	n.a.
M13_42	n.a.	n.a.	0.2023	0.512850	10	1.7	n.a.	n.a.	n.a.	n.a.
M13_43c	n.a.	n.a.	0.1589	0.511964	10	2.9	n.a.	n.a.	n.a.	n.a.
M13_43d	3.37	1.07	0.1918	0.512829	7	5.8	1.1418384	4E-06	−0.1	3.8
M13_54a	8.30	1.57	0.1144	0.511100	10	5.0	1.1418414	4E-06	3.2	3.4
M13_58*	0.66	0.18	0.1663	0.512436	7	9.0	n.a.	n.a.	n.a.	n.a.
M13_64a	n.a.	n.a.	0.1865	0.512480	8	1.2	n.a.	n.a.	n.a.	n.a.
M13_64b	12.35	3.40	0.1666	0.512264	9	5.5	1.1418369	4E-06	−0.7	3.2
M13_64c	3.35	0.95	0.1722	0.512379	8	5.4	n.a.	n.a.	n.a.	n.a.
M13_64e	0.35	0.11	0.1940	0.512807	8	4.4	n.a.	n.a.	n.a.	n.a.
M13_68b	8.76	2.49	0.1720	0.512344	6	4.8	1.1418259	3E-06	−3.5	2.9
M13_77b	0.82	0.22	0.1649	0.512243	7	5.8	n.a.	n.a.	n.a.	n.a.
M13_76a	n.a.	n.a.	0.1719	0.512267	7	3.3	n.a.	n.a.	n.a.	n.a.
M13_84	n.a.	n.a.	0.1838	0.512516	8	3.1	n.a.	n.a.	n.a.	n.a.
M13_101	0.82	0.25	0.1815	0.512515	7	4.1	n.a.	n.a.	n.a.	n.a.
M13_102	0.84	0.17	0.1214	0.511125	8	2.5	n.a.	n.a.	n.a.	n.a.
M13_105	n.a.	0.17	0.1864	0.512799	8	7.5	n.a.	n.a.	n.a.	n.a.

$\varepsilon^{143}Nd_i$ calculated with an age of 3300 Ma and CHUR ^{143}Nd of 0.512630 and Sm/Nd of 0.1960 (Bouvier et al., 2008). $\mu^{142}Nd$ calculated to terrestrial standard JNdi measured during same analytical session as the samples.

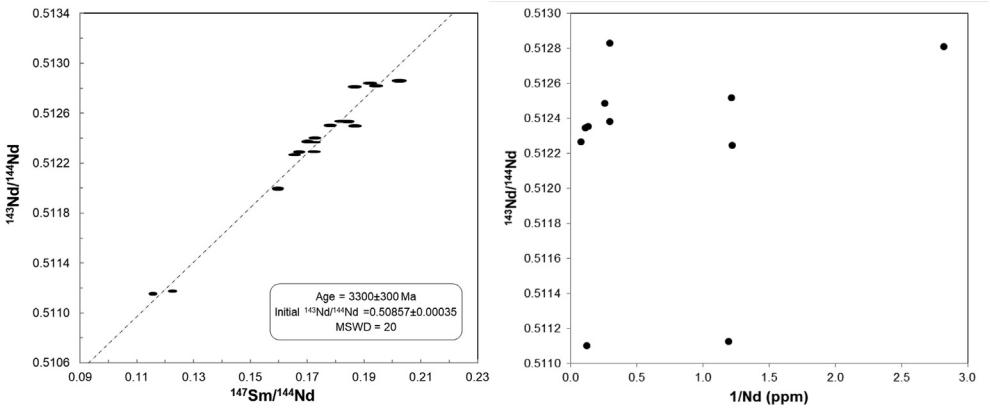

Fig. 8. a) 147Sm-143Nd isochron for 17 of the Amsaga meta-basalts. Data are presented in Table 2. Isochron calculated using IsoPlot (Ludwig, 2003). Ellipses are the 2σ error on the analysis. b) 143Nd/144Nd versus 1/Nd concentration, the lack of a correlation in this space shows that the errorchron is not related to binary mixing such as that expected due to crustal contamination.

Hoffman, 2003). These diagrams show that a number of elements have been modified by fluids, likely during metamorphism, most noticeably Th and Rb have been the most severely affected by post-eruption processes. Thorium is not usually fluid mobile, but has been affected by secondary processes in the Amsaga meta-basalts (Figs. 5 and 6).

The incompatible element plots look like typical modern arc signatures, with negative anomalies in the HFSE (Nb, Ta, Zr, Ti), and are enriched compared to Primitive Mantle by an order of magnitude (Fig. 7). Negative anomalies in Nb-Ta and Ti can be caused by crustal assimilation, but as discussed above the meta-basalts are unaffected by this process. The three elements also show correlations with Zr (Fig. 6), indicating they have been unaffected by secondary processes and display primary compositions, as such the depletions in the HFSE are most likely a source/melting feature. The extent of the depletions are very similar to other Archean terranes, with trace element patterns comparable to those observed in mafic rocks from Isua and Abitibi (Condie, 2005; Polat et al, 2011; van Hunen and Moyen, 2012), which have been interpreted to represent arc-like sequences. Nonetheless, it is important to note that a modern arc-like trace element signature in Archean rocks does not necessarily infer an arc-like setting. Rocks from the East Pilbara Terrane in Australia also display arc-like trace element profiles, but field evidence and other geochemical indicators imply that these were not formed in an arc setting (Johnson et al., 2017).

Seventeen of the meta-basalts of the Amsaga region produce a Sm-Nd errorchron with an age of 3300 ± 300 Ma (2σ, MSWD of 20; all 19 samples produce an errorchron of 3171 Ma ± 420, MSWD = 50). The large MSWD could be the result of metamorphic disturbance, non-isochronous samples or non-cogenetic samples. We showed that metamorphic disturbance is small, but likely exists at the precision level required for dating. This is evidenced by the improvement of the errorchron when removing two samples (M13_37 and M13_58) that plot further away from the regression line. It is indeed also unlikely that the meta-basalts would have formed from a single magma pulse, which is why only an errorchron can be produced and not an accurate age. On the other hand, the similar trace element systematics and correlations with Zr of the samples suggests that they are potentially genetically linked at the source. The age is also similar to some of the gneisses in the area, with U-Pb zircon ages are 3515 ± 15 Ma and 3422 ± 10 Ma (Potrel et al., 1996). The large error and MSWD imply that this age is neither accurate nor precise, nevertheless it still provides a time frame over which these meta-basalts were potentially erupted. The initial $^{143}Nd/^{144}Nd$ of the errorchron correlates to a positive εNd of + 4.4, while the age produces an average εNd_i for the samples of 4.9 ± 2.4. Using the maxima of the age shifts the εNd_i averages to 5.9 ± 2.7, while the minima gives 3.9 ± 2.4. These elevated and systematically positive within error εNd_i signifies that the source that produced the protolith melt was already significantly depleted during the Paleoarchean, in agreement with the Nd curve evolution of the depleted MORB mantle (DePaolo, 1981). The lack of any correlations between $^{143}Nd/^{144}Nd$ and 1/Nd (Fig. 8) further signifies that these samples are largely crustal contamination free and the errorchron is not a mixing line.

The preservation of a Paleoarchean age in the meta-basalts is further proof that these samples have not been significantly altered by post-eruption processes and their chemical signatures can be used to discuss Paleoarchean mantle dynamics.

6.2. Geodynamic setting for the formation of the Amsaga terrane

Recently, the sole use of geochemical parameters to determine the geological setting of Archean rocks has been called into question (Condie, 2005; Condie, 2015 and references herein). Condie (2015) suggests a combination of field associations, lithological units and geochemistry is required to make an accurate assessment of the tectonic setting. The Amsaga meta-basalts are found as lenses and dykes within the felsic rocks, with no ophiolite-like stratigraphic sequence observed. There are also no meta-sediments associated to either the meta-basalts or the TTGs. The combination of no stratigraphic sequence in the mafic rocks and a lack of sediments points to a non-arc related tectonic setting. Of course, as the Amsaga area is located in the Western Sahara of Mauritania, it is possible that some lithological units are covered by dense sand dunes.

The Amsaga meta-basalts have trace element profiles similar to modern arc basalts and other Archean greenstone terranes, such as from the Isua Supercrustal Belt (ISB; Greenland) and the Abitibi Greenstone Belt (Canada; Fig. 7). However, some of the Isua and Abitibi mafics also show a large negative anomaly in Sr that is not seen in the Amsaga samples. Nonetheless, a subset of Abitibi mafic rocks have a similar range in Sr anomalies as those observed in the Amsaga meta-basalts. These Abitibi samples have been interpreted as non-arc related units, and likely occurred in an intraplate setting (Moyen and van Hunen, 2012). On the other hand, the ISB has been interpreted as representing an Archean arc complex, based on the trace element characteristics such as depleted Sr, Nb-Ta and Ti, coupled with field relationships (Polat and Hofmann, 2003). In Zr/Nb versus Nb/Th space, the Amsaga meta-basalts, Abitibi mafics and ISB all plot towards more hydrated/continental sources (Fig. 9b). However, in a plot of Th/Yb versus Nb/Yb (Fig. 9a), both the Amsaga meta-basalts and Abitibi mafics fall just above the MORB-OIB array, quite removed from the arc array. In that plot, the ISB mafics form a trend with the majority of samples falling in the arc-array, reflecting the different geodynamical setting for the ISB compared to Abitibi. Nevertheless, these discrimination diagrams are based on Th, which has been affected by post-emplacement process in the Amsaga meta-basalts (see Section 6.1). As such, their interpretation remains inconclusive for the Amsaga.

In the present study, only the coupled depletion in Nb-Ta of the Amsaga meta-basalts indicates an arc-like formation. However, such chemical compositions can be indicators of other processes such as 1)

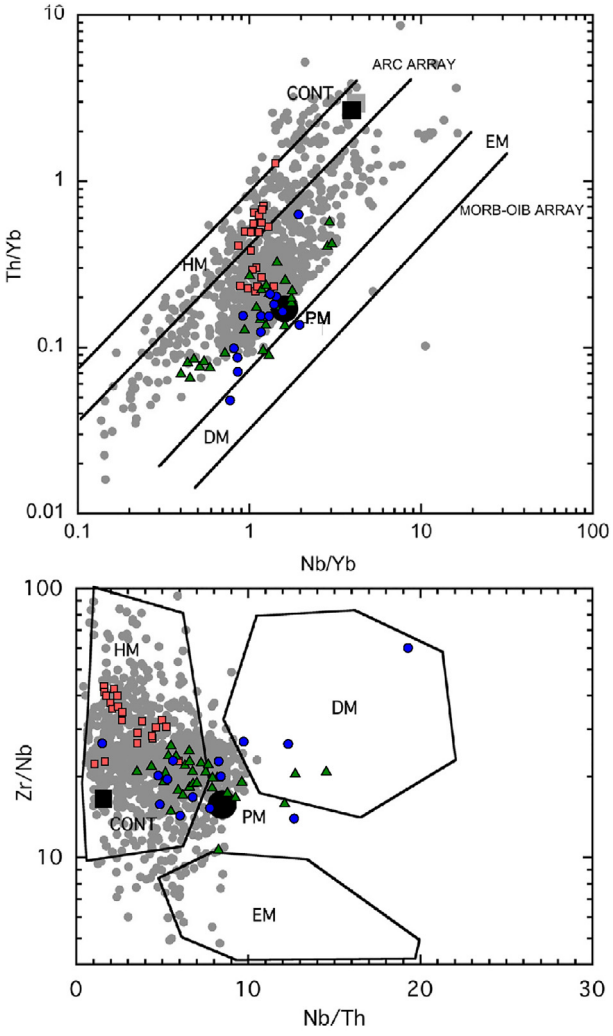

Fig. 9. Discrimination diagrams for different mantle sources from Condie and Shearer (2017), blue circles are Archean oceanic basalts from hydrated sources. Blue circles are the Amsaga meta-basalts, for comparison mafic rocks from Abitibi (green triangles; Dostal and Mueller, 2013; Kerrich et al 1999, 2008; Wyman 1999) and Isua (Red squares, Polat and Hofmann 2003) are also shown. Amsaga meta-basalts plot closer to the MORB-OIB array than the majority of Archean hydrated oceanic basalts. Bottom shows distribution of Amsaga meta-basalts in Zr/Nb and Nb/Th space. In this diagram, Amsaga meta-basalts are generally similar to samples from hydrated mantle sources. Fields from depleted mantle (DM), hydrated mantle (HM) and enriched mantle (EM) are also shown, the black circle is Primitive Mantle (PM) and the black square is the average continental crust.

contamination by pre-existing continental crust due to its high Th/Yb and Nb/Yb, 2) melting of an enriched source such as fertile peridotite would also yield an arc-like trace element signature (van Hunen and Moyen, 2012), or 3) Presence of rutile in either the production or evolution of the Amsaga magmas.. Contamination by continental crust has been ruled out based on trace element correlations and Nd isotopes (see Section 6.1), and therefore cannot be invoked as the reason for the trace element profile of the Amsaga meta-basalts. While the melting of a fertile source seems viable, the ^{143}Nd compositions measured in this study indicates that the source mantle was depleted at the time of extraction with an εNd_i of +4.4. Polat et al. (1999) noted that a fertile source is incompatible with a positive εNd_i of +4. The final hypothesis requires rutile which is commonly evoked to be the source of Nb-Ta and Ti depletions as it has a high partition co-efficient for both Nb and Ta but with a preference for Nb (Foley et al., 2000; Rapp et al., 2003; Xiong et al., 2005), so it is able to fractionate those two elements. Rutile would also have been stable above 1.2 GPa and 700 °C during the Archean (Johnson et al., 2017), even though it is not a primary mantle mineral. Nevertheless, there are three possible scenarios in which rutile could interact with the Amsaga magmas, 1) dehydration melting of a subducting slab, 2) delamination and subsequent remelting of mafic crust or 3) assimilation of mafic crust. Foley et al. (2000) demonstrated that dehydration melting of a rutile-bearing subducted slab can be the source for the HFSE fractionations seen in arc-basalts. This would require horizontal plate motion and subduction of a hydrated basaltic crust. On the other hand, Johnson et al. (2014) showed that at the base of a thick MgO rich ultramafic crust, rutile is stable while the base of the crust becomes negatively buoyant and delaminates. The delaminating crust interacts with the ambient mantle and produces basalts with lower MgO and fractionated Nb-Ta (Johnson et al., 2014). Such a thick crust should have been widespread in the Archean due to the hotter ambient mantle which could create stagnant lid conditions (Korenaga 2013; O'Neill and Debaille, 2014). One caveat of both these models is that garnet is also stable alongside rutile, which would result in fractionated REE. This is clearly not seen in the Amsaga meta-basalts and therefore either requires the presence of rutile without garnet or the total exhaustion of garnet during melting, which leaves the third scenario, assimilation of mafic crust. If a thick mafic crust existed during the Archean, it would have a very similar composition to the Amsaga magmas, with potentially very similar Nd compositions. Consequently, any contamination by such a crust would be difficult to isolate from the primary melt composition, except for some key mineral phases, as rutile. Addition of a small amount of this mafic crust through assimilation would potentially be enough to cause the depletions in Nb-Ta and Ti seen, while not greatly affecting the other trace elements or Nd compositions. Due to this similarity in compositions, determining if any mafic crustal contamination has occurred is thus difficult to assess and as such the trace element compositions of the Amsaga meta-basalts are unable to discriminate between the two endmember tectonic settings. This conclusion reinforces those from Condie (2015) who stated that trace element geochemical evidences are often not sufficient to conclude on the geodynamic setting.

6.3. Significance of the ^{142}Nd signature

The ^{143}Nd systematics of the Amsaga meta-basalts indicates that the source of the protolith had already undergone significant depletion by 3.4 Ga, based on the εNd_i of +4.4. However, no DMM model age can be obtained for Nd isotopes (using the DMM values from Workman and Hart, 2005). This clearly indicates that while the source of the Amsaga mafics was depleted, it does not correspond to the DMM as we know it today. In addition, there are no detectable ^{142}Nd anomalies, indicating that the differentiation of the source either occurred after the extinction of ^{146}Sm at around 4 Ga or that the source region was homogenised in terms of ^{142}Nd prior to subsequent enrichment in ^{143}Nd. As the geodynamical regime that created the Amsaga meta-basalts cannot be determined from the trace element compositions (Section 6.2), it is also difficult to differentiate between the two potential reasons for a lack of ^{142}Nd anomaly. If the initial differentiation event led to a smaller anomaly, as the one observed in Barberton komatiites (Puchtel et al., 2016), both a stagnant-lid slow mixing and a mobile-lid fast mixing could result in a homogeneous reservoir by 3.3 Ga in the Amsaga source (Debaille et al., 2013).

The lack of anomaly highlights a growing trend in the literature with regards to ^{142}Nd anomalies. To date, the only significant anomalies ($> \sim 8$ μ^{142}Nd; (Bennett et al., 2007; Boyet and Carlson, 2006; O'Neil et al., 2008; Puchtel et al., 2016; Rizo et al., 2011; Roth et al., 2013) detected in Archean terranes have been confined to the composite Proterozoic craton composed of the Superior, Slave and North Atlantic Cratons (Van Kranendonk et al., 1993; Zhao et al., 2004). There is very limited data available on any of the other cratons worldwide (Bennett et al., 2007; Caro et al., 2006; Puchtel et al., 2013,

2016; Schneider et al., 2018), but so far this limited data shows either no anomalies or very minor anomalies only one or two μ units from terrestrial. With the advent of similar sized anomalies found in modern day OIB basalts (Peters et al., 2018), their significance in determining the type of mantle dynamics in the Archean seems minimal.

7. Conclusion

The Amsaga meta-basalts have been metamorphosed to granulite and retrograde amphibolite facies, but retain a number of primary geochemical signatures. Trace element signatures are similar to other mafic rocks from Archean aged terranes across the world, with depletions in Nb-Ta and Ti, and relatively unfractionated REE. However, those geochemical signatures cannot be used as diagnostic of the geodynamical setting. Indeed, Th has been shown to be mobile in our samples. In any case, contamination by the continental crust seems minimal. Indeed, the meta-basalts preserve a $^{143}Nd/^{144}Nd$ errorchron with an age of 3300 ± 300 Ma and an eNd_i of + 4.4, consistent with the temporal evolution of the DMM. No anomalous ^{142}Nd signature was determined in the meta-basalts, indicating that any signature of early differentiation had been homogenised prior to formation of the meta-basalts. Again, this information cannot be used to infer the geodynamical regime. Regarding the Amsaga meta-basalts, several contradictory characteristics remain unresolved, including the combination of a depleted Nd isotope signature with a negative Nb-Ta typical of an enriched source.

Acknowledgments

ANW thanks the ERC StG “ISoSyC” for funding. FEA, NM and VD thank the BELSPO IUAP Planet-Topers for past funding, and for funding the field mission. Julien Berger is warmly thanked for his help on the field. Sabrina Cauchies and Wendy Debouge are thanked for assisting in the lab, and Rosalind Armytage for helping with Nd measurements. VD thanks the ERC StG “ISoSyC” and FRS-FNRS for present support.

Appendix A. Supplementary data

Supplementary data to this article can be found online at https://doi.org/10.1016/j.precamres.2019.02.005.

References

Abouchami, W., Boher, M., Michard, A., Albarede, F., 1990. A major 2.1 Ga event of mafic magmatism in West Africa: an early stage of crustal accretion. J. Geophys. Res.: Solid Earth (1978–2012), 95, 17605–17629.

Anders, E., Grevesse, N., 1989. Abundances of the elements: Meteoritic and solar. Geochim. Cosmochim. Acta 53, 197–214. https://doi.org/10.1016/0016-7037(89)90286-X.

Auvray, B., Peucat, J.J., Potrel, A., Burg, J.P., Caruba, C., Lo, K., 1992. Données géochronologiques nouvelles sur l’Archéen de l’Amsaga (Dorsale Réguibat, Mauritanie). Comptes Rendues de l’Académie des Sciences de Paris 315, 63–70.

Bédard, J.H., 2018. Stagnant lids and mantle overturns: Implications for Archaean tectonics, magmagenesis, crustal growth, mantle evolution, and the start of plate tectonics. Geosci. Front Lid Tectonics 9, 19–49. https://doi.org/10.1016/j.gsf.2017.01.005.

Bédard, J.H., Harris, L.B., Thurston, P.C., 2013. The hunting of the snArc. Precambrian Res. Evolving Early Earth 229, 20–48. https://doi.org/10.1016/j.precamres.2012.04.001.

Bennett, V.C., Brandon, A.D., Nutman, A.P., 2007. Coupled 142Nd-143Nd Isotopic Evidence for Hadean Mantle Dynamics. Science 318, 1907–1910. https://doi.org/10.1126/science.1145928.

Berger, J., Diot, H., Lo, K., Ohnenstetter, D., Féménias, O., Pivin, M., Demaiffe, D., Bernard, A., Charlier, B., 2013. Petrogenesis of Archean PGM-bearing chromitites and associated ultramafic–mafic–anorthositic rocks from the Guelb el Azib layered complex (West African craton, Mauritania). Precambr. Res. 224, 612–628.

Boher, M., Abouchami, W., Michard, A., Albarède, F., Arndt, N., 1992. Crustal growth in West Africa at 2.1 Ga. J. Geophys. Res. 97, 345–369.

Bourdon, B., Caro, G., 2007. The early terrestrial crust. Comptes Rendus Geosci. Formation du système solaire : approche cosmochimique dans le conteste astrophysique 339, 928–936. https://doi.org/10.1016/j.crte.2007.09.002.

Bouvier, A., Vervoort, J.D., Patchett, P.J., 2008. The Lu–Hf and Sm–Nd isotopic composition of CHUR: constraints from unequilibrated chondrites and implications for the bulk composition of terrestrial planets. Earth Planet. Sci. Lett. 273, 48–57. https://doi.org/10.1016/j.epsl.2008.06.010.

Boyet, M., Carlson, R., 2006. A new geochemical model for the Earth’s mantle inferred from 146Sm–142Nd systematics. Earth Planet. Sci. Lett. 250, 254–268. https://doi.org/10.1016/j.epsl.2006.07.046.

Caro, G., Bourdon, B., Birck, J.-L., Moorbath, S., 2006. High-precision 142Nd/144Nd measurements in terrestrial rocks: constraints on the early differentiation of the Earth’s mantle. Geochim. Cosmochim. Acta 70, 164–191. https://doi.org/10.1016/j.gca.2005.08.015.

Caro, G., Bourdon, B., Wood, B.J., Corgne, A., 2005. Trace-element fractionation in Hadean mantle generated by melt segregation from a magma ocean. Nature 436, 246–249. https://doi.org/10.1038/nature03827.

Caro, G., Morino, P., Mojzsis, S.J., Cates, N.L., Bleeker, W., 2017. Sluggish Hadean geodynamics: evidence from coupled 146,147Sm–142,143Nd systematics in Eoarchean supracrustal rocks of the Inukjuak domain (Québec). Earth Planet. Sci. Lett. 457, 23–37. https://doi.org/10.1016/j.epsl.2016.09.051.

Chauvel, C., Blichert-Toft, J., 2001. A hafnium isotope and trace element perspective on melting of the depleted mantle. Earth Planet. Sci. Lett. 190, 137–151. https://doi.org/10.1016/S0012-821X(01)00379-X.

Condie, K., 2005. High field strength element ratios in Archean basalts: a window to evolving sources of mantle plumes? Lithos 79, 491–504. https://doi.org/10.1016/j.lithos.2004.09.014.

Condie, K., 2015. Changing tectonic settings through time: Indiscriminate use of geochemical discriminant diagrams. Precambrian Res. 266, 587–591. https://doi.org/10.1016/j.precamres.2015.05.004.

Condie, K.C., Shearer, C.K., 2017. Tracking the evolution of mantle sources with incompatible element ratios in stagnant-lid and plate-tectonic planets. Geochim. Cosmochim. Acta 213, 47–62. https://doi.org/10.1016/j.gca.2017.06.034.

Debaille, V., Brandon, A.D., Yin, Q.Z., Jacobsen, B., 2007. Coupled 142Nd–143Nd evidence for a protracted magma ocean in Mars. Nature 450, 525–528. https://doi.org/10.1038/nature06317.

Debaille, V., O’Neill, C., Brandon, A.D., Haenecour, P., Yin, Q.-Z., Mattielli, N., Treiman, A.H., 2013. Stagnant-lid tectonics in early Earth revealed by 142Nd variations in late Archean rocks. Earth Planet. Sci. Lett. 373, 83–92. https://doi.org/10.1016/j.epsl.2013.04.016.

DeJoux, A., Thordarson, T., Fitton, J.G., Hastie, A.R., 2014. The Cosmos greenstone succession, Agnew-Wiluna greenstone belt, Yilgarn Craton, Western Australia: geochemistry of an enriched Neoarchean volcanic arc succession. Lithos 205, 148–167. https://doi.org/10.1016/j.lithos.2014.06.013.

DePaolo, D.J., 1981. Trace element and isotopic effects of combined wallrock assimilation and fractional crystallization. Earth. Planet. Sci. Lett. 53, 189–202. https://doi.org/10.1016/0012-821X(81)90153-9.

Dostal, J., Mueller, W.U., 2013. Deciphering an Archean mantle plume: Abitibi greenstone belt, Canada. Gondwana Res. 23, 493–505. https://doi.org/10.1016/j.gr.2012.02.005.

Foley, S.F., Barth, M.G., Jenner, G.A., 2000. Rutile/melt partition coefficients for trace elements and an assessment of the influence of rutile on the trace element characteristics of subduction zone magmas - ScienceDirect. Geochim. Cosmochim. Acta 64, 933–938. https://doi.org/10.1016/S0016-7037(99)00355-5.

van Hunen, J., Moyen, J.-F., 2012. Archean Subduction: Fact or Fiction? Annu. Rev. Earth Planet. Sci. 40, 195–219. https://doi.org/10.1146/annurev-earth-042711-105255.

Johnson, T.E., Brown, M., Kaus, B.J.P., VanTongeren, J.A., 2014. Delamination and recycling of Archaean crust caused by gravitational instabilities. Nat. Geosci. 7, 47–52. https://doi.org/10.1038/ngeo2019.

Johnson, T.E., Brown, M., Gardiner, N.J., Kirkland, C.L., Smithies, R.H., 2017. Earth's first stable continents did not form by subduction. Nature 543, 239–242. https://doi.org/10.1038/nature21383.

Johnson, T.E., Gardiner, N.J., Miljković, K., Spencer, C.J., Kirkland, C.L., Bland, P.A., Smithies, R.H., 2018. An impact melt origin for Earth’s oldest known evolved rocks. Nat. Geosci. 11, 795–799. https://doi.org/10.1038/s41561-018-0206-5.

Kerrich, R., Polat, A., Wyman, D., Hollings, P., 1999. Trace element systematics of Mg-, to Fe-tholeiitic basalt suites of the Superior Province: implications for Archean mantle reservoirs and greenstone belt genesis. Lithos 46, 163–187. https://doi.org/10.1016/S0024-4937(98)00059-0.

Kerrich, R., Polat, A., Xie, Q., 2008. Geochemical systematics of 2.7 Ga Kinojevis Group (Abitibi), and Manitouwadge and Winston Lake (Wawa) Fe-rich basalt–rhyolite associations: Backarc rift oceanic crust? Lithos 101, 1–23. https://doi.org/10.1016/j.lithos.2007.07.009.

Key, R.M., Loughlin, S.C., Gillespie, M., Del Rio, M., Horstwood, M.S.A., Crowley, Q.G., Darbyshire, D.P.F., Pitfield, P.E.J., Henney, P.J., 2008. Two Mesoarchaean terranes in the Reguibat shield of NW Mauritania. Geological Society of London, Special Publications 297, 33–52.

Korenaga, J., 2013. Initiation and Evolution of Plate Tectonics on Earth: Theories and Observations. Annu. Rev. Earth Planet. Sci. 41, 117–151. https://doi.org/10.1146/annurev-earth-050212-124208.

Korenaga, J., 2008. Urey ratio and the structure and evolution of Earth’s mantle. Rev. Geophys. 46. https://doi.org/10.1029/2007RG000241.

Li, C.-F., Wang, X.-C., Li, Y.-L., Chu, Z.-Y., Guo, J.-H., Li, X.H., 2014. Ce-Nd separation by solid phase micro-extraction and its application to high-precision 142Nd/144Nd measurements using TIMS in geological materials. J. Anal. At. Spectrom. 30, 895–902. https://doi.org/10.1039/C4JA00328D.

Ludwig, K.R., 2003. User's manual for Isoplot 3.00. A geochronological Toolkit for Microsoft Excel. Berkeley Geochronology Center, Special Publication No. 4a, Berkeley, California.

McDonough, W.F., Sun, S.-S., 1995. The composition of the Earth. Chem. Geol. 120,

223–253. https://doi.org/10.1016/0009-2541(94)00140-4.
Moyen, J.-F., van Hunen, J., 2012. Short-term episodicity of Archaean plate tectonics. Geology 40, 451–454. https://doi.org/10.1130/G322894.1.
O'Neil, J., Carlson, R.W., Francis, D., Stevenson, R.K., 2008. Neodymium-142 Evidence for Hadean Mafic Crust. Science 321, 1828–1831. https://doi.org/10.1126/science.1161925.
O'Neill, C., Debaille, V., Griffin, W.L., 2013. Deep Earth recycling in the Hadean and constraints on surface tectonics. Am. J. Sci. 313 (9), 912–932. https://doi.org/10.2475/09.2013.04.
O'Neill, C., Debaille, V., 2014. The evolution of Hadean-Eoarchaean geodynamics. Earth Planet. Sci. Lett. 406, 49–58. https://doi.org/10.1016/j.epsl.2014.08.034.
Ordóñez-Calderón, J.C., Polat, A., Fryer, B.J., Gagnon, J.E., Raith, J.G., Appel, P.W.U., 2008. Evidence for HFSE and REE mobility during calc-silicate metasomatism, Mesoarchean (~3075Ma) Ivisaartoq greenstone belt, southern West Greenland. Precambrian Res. 161, 317–340. https://doi.org/10.1016/j.precamres.2007.09.004.
Peters, B.J., Carlson, R.W., Day, J.M.D., Horan, M.F., 2018. Hadean silicate differentiation preserved by anomalous $^{142}Nd/^{144}Nd$ ratios in the Réunion hotspot source. Nature 555, 89–93. https://doi.org/10.1038/nature25754.
Polat, A., Hofmann, A.W., 2003. Alteration and geochemical patterns in the 3.7–3.8 Ga Isua greenstone belt, West Greenland. Precambr. Res. 126 (3), 197–218.
Polat, A., Kerrich, R., Wyman, D.A., 1999. Geochemical diversity in oceanice komatiites and basalts from the late Archean Wawa greenstone belts, Superior Province, Canada: trace element and Nd isotope evidence for a heterogeneous mantle. Precambr. Res. 94, 139–173.
Polat, A., Appel, P.W., Fryer, B.J., 2011. An overview of the geochemistry of Eoarchean to Mesoarchean ultramafic to mafic volcanic rocks, SW Greenland: implications for mantle depletion and petrogenetic processes at subduction zones in the early Earth. Gondwana Res. 20 (2), 255–283.
Potrel, A., 1994. Evolution tectono-métamorphique d'un segment de croûte continentale archéenne. Exemple de l'Amsaga (R.I. Mauritanie), Dorsale Réguibat (craton Ouest Africain). Thèse de doctorat, Rennes, France, p. 400.
Potrel, A., Peucat, J.J., Fanning, C.M., Auvray, B., Burg, J.P., Caruba, C., 1996. 3.5 Ga old terranes in the West African Craton, Mauritania. J. Geol. Soc. 153, 507–510.
Potrel, A., Peucat, J.J., Fanning, C.M., 1998. Archean crustal evolution of the west African craton: example of the Amsaga area (Reguibat rise). U-Pb and Sm–Nd evidence for crustal growth and recycling. Precambr. Res. 90, 107–117.
Puchtel, I.S., Blichert-Toft, J., Touboul, M., Horan, M.F., Walker, R.J., 2016. The coupled ^{182}W- ^{142}Nd record of early terrestrial mantle differentiation: early mantle differentiation. Geochem. Geophys. Geosyst. 17, 2168–2193. https://doi.org/10.1002/2016GC006324.
Puchtel, I.S., Blichert-Toft, J., Touboul, M., Walker, R.J., Byerly, G.R., Nisbet, E.G., Anhaeusser, C.R., 2013. Insights into early Earth from Barberton komatiites: Evidence from lithophile isotope and trace element systematics. Geochim. Cosmochim. Acta 108, 63–90. https://doi.org/10.1016/j.gca.2013.01.016.
Rapp, R.P., Shimizu, N., Norman, M.D., 2003. Growth of early continental crust by partial melting of eclogite. Nature 425, 605–609. https://doi.org/10.1038/nature02031.
Rizo, H., Boyet, M., Blichert-Toft, J., Rosing, M., 2011. Combined Nd and Hf isotope evidence for deep-seated source of Isua lavas. Earth Planet. Sci. Lett. 312, 267–279. https://doi.org/10.1016/j.epsl.2011.10.014.
Roth, A.S.G., Bourdon, B., Mojzsis, S.J., Touboul, M., Sprung, P., Guitreau, M., Blichert-Toft, J., 2013. Inherited 142Nd anomalies in Eoarchean protoliths. Earth Planet. Sci. Lett. 361, 50–57. https://doi.org/10.1016/j.epsl.2012.11.023.
Schneider, K.P., Hoffmann, J.E., Boyet, M., Münker, C., Kröner, A., 2018. Coexistence of enriched and modern-like 142Nd signatures in Archean igneous rocks of the eastern Kaapvaal Craton, southern Africa. Earth Planet. Sci. Lett. 487, 54–66. https://doi.org/10.1016/j.epsl.2018.01.022.
Smithies, R.H., Champion, D.C., Van Kranendonk, M.J., Howard, H.M., Hickman, A.H., 2005. Modern-style subduction processes in the Mesoarchean: geochemical evidence from the 3.12 Ga Whundo intra-oceanic arc. Earth. Planet. Sci. Lett. 231, 221–237. https://doi.org/10.1016/j.epsl.2004.12.026.
Szilas, K., Naeraa, T., Schersten, A., Stendal, H., Frei, R., van Hinsberg, V.J., Kokfelt, T.F., Rosing, M.T., 2012. Origin of Mesoarchean arc-related rocks with boninite/komatiite affinities from southern West Greenland. Lithos 144–145, 24–39. https://doi.org/10.1016/j.lithos.2012.03.023.
Touboul, M., Puchtel, I.S., Walker, R.J., 2012. 182W Evidence for Long-Term Preservation of Early Mantle Differentiation Products. Science 335, 1065–1069. https://doi.org/10.1126/science.1216351.
Van Kranendonk, M.J., St-Onge, M.R., Henderson, J.R., 1993. Paleoproterozoic tectonic assembly of Northeast Laurentia through multiple indentations. Precambrian Res. 63, 325–347. https://doi.org/10.1016/0301-9268(93)90039-5.
Willbold, M., Mojzsis, S.J., Chen, H.-W., Elliott, T., 2015. Tungsten isotope composition of the Acasta Gneiss Complex. Earth Planet. Sci. Lett. 419, 168–177. https://doi.org/10.1016/j.epsl.2015.02.040.
Winchester, J.A., Floyd, P.A., 1977. Geochemical discrimination of different magma series and their differentiation products using immobile elements. Chem. Geol. 20, 325–343.
Workman, R.K., Hart, S.H., 2005. Major and trace element composition of the depleted MORB mantle (DMM). Earth. Planet. Sci. Lett. 231, 53–72. https://doi.org/10.1016/j.epsl.2004.12.005.
Wyman, D.A., 1999. A 2.7 Ga depleted tholeiite suite: evidence of plume-arc interaction in the Abitibi Greenstone Belt, Canada. Precambrian Res. 97, 27–42. https://doi.org/10.1016/S0301-9268(99)00018-2.
Xiong, X.L., Adam, J., Green, T.H., 2005. Rutile stability and rutile/melt HFSE partitioning during partial melting of hydrous basalt: implications for TTG genesis. Chem. Geol. 218, 339–359. https://doi.org/10.1016/j.chemgeo.2005.01.014.
Zhao, G., Sun, M., Wilde, S.A., Li, S., 2004. A Paleo-Mesoproterozoic supercontinent: assembly, growth and breakup. Earth-Sci. Rev. 67, 91–123. https://doi.org/10.1016/j.earscirev.2004.02.003.